Chinese Chemical Letters 36 (2025) 110041

Contents lists available at ScienceDirect

Chinese Chemical Letters

journal homepage: www.elsevier.com/locate/cclet

Direct regeneration of spent $LiFePO_4$ cathode material *via* a simple solid-phase method

Hao Sun[a], Xiaoxue Li[a], Baoyu Wu[a], Kai Zhu[a,*], Yinyi Gao[a], Tianzeng Bao[b], Hongbin Wu[b], Dianxue Cao[a,*]

[a] Key Laboratory of Superlight Materials and Surface Technology of Ministry of Education, College of Materials Science and Chemical Engineering, Harbin Engineering University, Harbin 150001, China
[b] Hunan Hongshan New Energy Technology Co., Ltd., Yiyang 413000, China

ARTICLE INFO

Article history:
Received 24 January 2024
Revised 27 February 2024
Accepted 22 May 2024
Available online 22 May 2024

Keywords:
Spent $LiFePO_4$
Carbon dioxide
Carbon coating
Lithium-iron antiphase defects
Direct regeneration

ABSTRACT

For realizing the goals of "carbon peak" and "carbon neutrality", lithium-ion batteries (LIB) with $LiFePO_4$ as the cathode material have been widely applied. However, this has also led to a large number of spent lithium-ion batteries, and the safe disposal of spent lithium-ion batteries is an urgent issue. Currently, the main reason for the capacity decay of $LiFePO_4$ materials is the Li deficiency and the formation of the Fe^{3+} phase. In order to address this issue, we performed high-temperature calcination of the discarded lithium iron phosphate cathode material in a carbon dioxide environment to reduce or partially remove the carbon coating on its surface. Subsequently, mechanical grinding was conducted to ensure thorough mixing of the lithium source with the discarded lithium iron phosphate. The reaction between CO_2 and the carbon coating produced a reducing atmosphere, reducing Fe^{3+} to Fe^{2+} and thereby reducing the content of Fe^{3+}. The Fe^{3+} content in the repaired $LiFePO_4$ material is reduced. The crystal structure of spent $LiFePO_4$ cathode materials was repaired more completely compare with the traditional pretreatment method, and the repaired $LiFePO_4$ material shows good electrochemical performance and cycling stability. Under 0.1 C conditions, the initial capacity can reach 149.1 mAh/g. It can be reintroduced for commercial use.

In the context of increasingly scarce global resources, reducing resource consumption and environmental pollution is gradually becoming a widespread consensus among people [1-3]. Lithium-ion batteries (LIBs) are widely used due to their numerous advantages such as high energy density, low self-discharge, long cycling life, wide working temperature range, and excellent reliability. These benefits not only contribute to environmental protection but also help address energy storage challenges [4-6]. Among various lithium-ion batteries (LIBs), batteries with lithium iron phosphate ($LiFePO_4$, LFP) as the cathode material have gained significant attention due to their high safety, long lifespan, good high-temperature stability, and relatively low cost [7,8]. However, with the large-scale application of lithium-ion batteries (LIBs), the global lithium resource consumption has been increasing at an annual rate of 8% in recent years [9], and a large number of waste LIBs will be generated in the next five to ten years. By 2023, there will be 313.3 thousand tons of waste LIBs that need to be recycled. However, battery-grade lithium materials are limited, and the price of Li_2CO_3 has been on an upward trend, so the recycling of end-of-life lithium-ion batteries has a greater development prospect in terms of economy as well as resource utilization. Battery recycling and harmless treatment have become urgent issues that people need to address [10-13].

Currently, lithium-ion battery recycling technologies include pyrometallurgical recycling, hydrometallurgical recycling, and solid-phase direct regeneration [14-18]. The main recycling direction is the recovery of lithium and other valuable metals. For spent LFP, the lithium element must be recycled due to its relatively high value. Pyrometallurgical recycling technology utilizes high-temperature pyrolysis and mechanical separation methods to directly recover waste materials and metals, However, the entire production process consumes a large amount of energy, and the recovery of the lithium is not complete [14,19,20]. Therefore, it is unsuitable for recycling spent LFP. Hydrometallurgical recycling technology utilizes the strong acidic and alkaline solutions to separate metal ions from spent battery materials. Subsequently, the metal ions are converted into salts or oxides through processes such as ion exchange, precipitation, and adsorption, thereby achieving

* Corresponding authors.
E-mail addresses: kzhu@hrbeu.edu.cn (K. Zhu), caodianxue@hrbeu.edu.cn (D. Cao).

https://doi.org/10.1016/j.cclet.2024.110041
1001-8417/

the recovery of metal ions [21,22]. For instance, Yang *et al.* [23] achieved the recovery of Li and Fe from LFP cathode powder using a mechanochemical activation-based approach. However, the use of large amounts of strong acids, bases and other chemical reagents in the hydrometallurgical recycling process can easily cause pollution, and the process flow is long, with high repair and regeneration costs [24,25].

Compared with pyrometallurgical and hydrometallurgical recycling, direct regeneration does not produce any secondary pollution and has a short process flow, which is the most direct and effective recycling method. Liquid-phase direct regeneration is generally carried out by hydrothermal methods for lithium replenishment and repair. For example, Jia *et al.* [26] constructed a heterojunction interface between LFP and nitrogen-doped carbon, which increased the d-band center of Fe atoms. With the assistance of ethanol, LFP was repaired and maintained stable performance even at a current density of 10 C. Tang *et al.* [27] used L–serine as a reducing agent to repair LFP, and the capacity can still reach 147.9 mAh/g at a current density of 1 C. However, hydrothermal repair methods have high requirements for equipment due to high temperature and high pressure, have a small processing capacity, and are not easy to achieve industrial production. Compared with solid-phase regeneration, the samples obtained by the liquid-phase method have uniform particles and the reactions are easier to carry out. However, the liquid-phase method requires high temperature and high pressure, resulting in excessive equipment demands and limited processing capacity, thus lacking in industrial scalability compared to the solid-phase regeneration method.

Solid-phase direct regeneration involves mixing the lithium-deficient cathode materials with a lithium source, followed by high-temperature calcination, gradually embedding lithium into the lattice of the waste cathode materials to achieve the recovery of spent LFP. And the process requirements are low, suitable for industrial production. Li *et al.* [28] successfully repaired discarded LFP (lithium iron phosphate) using a direct regeneration method, achieving green recycling of the discarded LFP. The recycled material can be charged and discharged up to 147.3 mAh/g for the first time at 0.2 C. Chen *et al.* [29] employed a high-temperature solid-state regeneration method, utilizing lithium carbonate and glucose, to accomplish the repair of LFP. The recycled material can be charged and discharged up to 161.6 mAh/g for the first time at 0.1 C. The recycled LFP materials can be reused after repair, demonstrating the great potential of direct regeneration in the recycling of spent lithium-ion batteries [30-32].

The solid-phase direct regeneration method requires thorough contact between the lithium source and the material, thus traditional direct regeneration approaches necessitate a relatively long period of physical grinding during lithium source addition, typically requires 4–8 h of grinding, resulting in significant energy consumption during this stage. This study believe that the presence of a carbon coating hinders the replenishment of lithium sources, leading to prolonged physical grinding and increased energy consumption. Therefore, in our study, the carbon coating on the surface of spent lithium-ion batteries was thinned or partially removed by heat pretreatment in a CO_2 environment. Then the short-term physical milling method was combined with high-temperature thermal repair to make Li^+ more accessible to the corresponding crystal structure sites, thus completing the repair of the spent lithium iron phosphate materials.

In this study, we opted to utilize retired lithium-ion batteries obtained from automobiles. The retired lithium-ion batteries were recycled using a three-step process (Fig. 1). Firstly, the battery is discharged and dismantled to separate the aluminum foil current collector from the $LiFePO_4$ powder under oxygen-free calcination, resulting in retired $LiFePO_4$ (LFP(S)). Subsequently, LFP(S) was subjected to high-temperature calcination in a carbon dioxide gas environment to remove PVDF and thin or partially remove the carbon coating, while simultaneously reducing Fe^{3+} to Fe^{2+}. Finally, through a brief physical grinding process, lithium iron phosphate was thoroughly mixed with the lithium source, followed by high-temperature calcination, ultimately resulting in regenerated lithium iron phosphate material. The regenerated $LiFePO_4$ material (LFP(R)) has its crystal lattice restored, and the missing lithium elements are replenished. The lithium ion diffusion pathways are successfully unblocked, demonstrating higher capacity and capacity retention in electrochemical performance testing. Therefore, this study provides a low-energy and feasible method for regenerating $LiFePO_4$ materials, which holds promise for industrial battery recycling applications.

Discarded LIB was provided by Harbin Guangyu Battery Co., Ltd. The uncoated commercial $LiFePO_4$ was provided by Saiber Electrochemical Materials Co., Ltd., while super P was provided by Zhangjiagang City Guotai Huarong Chemical New Material Co., Ltd. The *N*-methylpyrrolidone (NMP) and polyvinylidene fluoride (PVDF) were provided by Guangdong Zhuguang New Energy Technology Co., Ltd.

The recycling and repair process of spent $LiFePO_4$ is shown in Fig. 1. The spent $LiFePO_4$ powder used in this study was obtained from spent LIB. Before dismantling the battery steel shell, the spent LIB was pre-treated by discharging to below 1 V to eliminate unnecessary dangers caused by dismantling. The spent LIB was manually dismantled using a steel saw and knife in a fume hood to obtain the battery core. Subsequently, the battery core was disassembled to obtain the cathode and anode plates. The obtained cathode plate is illustrated in Fig. S1 (Supporting information). The disassembled cathode plate was placed in a drying cabinet for dehydration, removing the electrolyte from the cathode plate. Due to severe damage to the discarded cathode plate, low-temperature calcination was employed to obtain discarded lithium iron phosphate powder. Onsequently, the cathode foil was cut into 2 cm × 2 cm square pieces, which were then heated in a tube furnace under an inert gas atmosphere to 400 °C and held for 1 h. At this point, the cathode material separated from the aluminum foil current collector, resulting in the obtained waste $LiFePO_4$ powder (LFP(S)) containing impurities such as PVDF.

The recovered cathode mixture (LFP(S)) was heated to 700 °C by a tube furnace and held for 4 h to achieve the removal of polyvinylidene fluoride (PVDF), and the high-temperature heating environments were filled with argon and carbon dioxide gases, respectively.

The elemental content of the S-LFP powder was determined by ICP-OES, allowing for the determination of the molar ratio of the main elements in $LiFePO_4$, and Li_2CO_3 was added according to the molar ratio that could restore the molar ratio of Li:Fe:P to 1.05:1:1, and then milled and mixed, grinding time 30 min, and then heated to 700 °C under a mixed hydrogen-argon atmosphere and held for 8 h. According to different impurity treatment methods, the samples calcined in hydrogen-argon mixed atmosphere are named as LFP(R)-Ar and LFP(R)-CO_2, respectively.

The above calcination conditions involve a heating rate of 5 °C/min, and the gas introduction rate is determined by the appearance of one tail gas bubble per second. The cooling process proceeds naturally. In the context of high-temperature calcination in a carbon dioxide environment, addressing the generation of CO tail gas, we employed the method illustrated in Fig. S2 (Supporting information). By igniting with oxygen, we successfully converted CO back into CO_2, achieving a closed-loop system.

The elemental content of the samples was quantified by inductively coupled plasma emission spectroscopy (ICP-OES, ICAP-7400, USA). The weight loss of the samples as a function of temperature was determined by thermogravimetric analyzer. The elemental valence of the materials was determined using an X-ray pho-

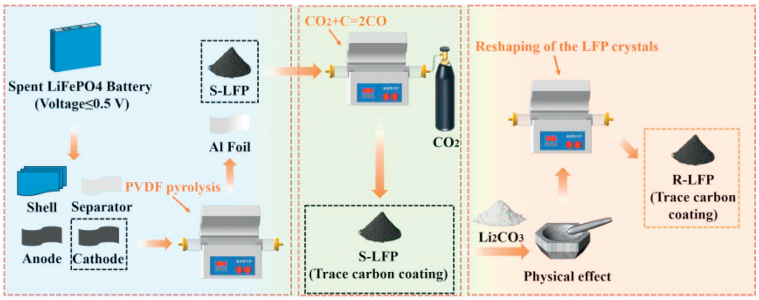

Fig. 1. Schematic diagram of the direct regeneration process for spent $LiFePO_4$.

toelectron spectroscope (XPS, Escalab Xi$^+$, USA), and the bonding category was identified. Determination of the substance classes and crystal structures contained in the samples by X-ray diffractometer (XRD, D: max-TTR III, Japan). Materials morphology and microstructural features were investigated using scanning electron microscopy (SEM, APREO S LOVAC, USA) and transmission electron microscopy (TEM, TECNAI F30).

The working electrode was prepared by mixing 80% of the regenerated cathode material, 10% of the conductive agent (Super-P), and 10% of the binder (PVDF) in NMP. The obtained mixture was coated onto aluminum foil and subjected to rolling, followed by drying in a vacuum environment at 80 °C for 12 h. With a mass loading of the active material of a *p*-proximately 1 mg, and the mass loading of the active material should not fluctuate by more than 0.1 mg. The resulting film was then assembled into a button-type half-cell within a glove box with water oxygen content below 0.5 ppm. Lithium foil was employed as the anode, and the electrolyte solution used was LB-002, which is a 1 mol/L $LiPF_6$ in a mixture of ethylene carbonate (EC) and dimethyl carbonate (DMC) (volume ratio of 1:1). Place the button cell in a constant temperature incubator or chamber at a temperature of 27 °C during the testing process to minimize the effects of environmental temperature fluctuations. The constant current charge/discharge tests were conducted in the voltage range of 2.8–4.2 V using a Neware battery testing system, at different current densities ranging from 0.1 C to 2 C (1 C = 170 mAh/g), for the electrochemical testing. Cycle voltammetry (CV) and electrochemical impedance spectroscopy (EIS) tests were carried out within a voltage range of 2.8–4.2 V using a Dutch electrochemical workstation.

Generally, the damage to the crystal structure of the cathode material and the loss of lithium are the direct causes of performance degradation in lithium-ion batteries [33,34]. The formation of "dead Li" [35,36] also resulted in less and less active lithium, resulting in a decrease in battery capacity. At the same time, the reduction of lithium content would cause the formation of Fe^{3+} in the crystal structure, thus inducing some lithium-iron antiphase defects [37-39], which would also hinder the migration of lithium ions. The damage to the crystal structure is due to the irreversible structural transformation of the original crystal structure caused by the absence of lithium [40,41]. This results in changes in volume and phase, leading to the blockage of lithium ion diffusion channels, reduction of ion diffusion rate, and increase in polarization reactions, thereby limiting the reaction kinetics and rate characteristics (Fig. 2a).

Inductively coupled plasma optical emission spectrometry (ICP-OES) and carbon-sulfur analyzer were employed to detect the elemental content of each sample. According to the data in Table S1 (Supporting information), the elemental content of Fe, Li, and P in LFP(S) is 12.75%, 1.297%, and 5.736%, respectively, with a carbon content of 4.3263%. The higher carbon content may be due to the presence of conductive agents in the waste lithium iron phosphate and the decomposition of PVDF. After restoration, the elemental content of Fe, Li, and P in LFP(R)-CO_2 is 4.296%, 0.6143%, and 2.233% respectively, and the n(Li):n(Fe):n(P) ratio changes from 0.82:1:0.82 to 1.15:1:0.94. The replenishment of lithium source is conducive to reducing lithium-iron anti-site defects, and the carbon content also decreases to 2.6698%, indicating that the carbon coating is thinned or partially detached after treatment with carbon dioxide.

X-ray photoelectron spectroscopy (XPS) is employed to identify the types of elemental species present on the surface of LFP and to assess the variations in the valence states of the surface elements in LFP. As shown in Fig. 2b, the XPS photoelectron spectroscopy of LFP(S), LFP(R)-Ar, LFP(R)-CO_2, and LFP(C) clearly reveals the elemental peaks of P 2s, C 1s, O 1s, and Fe 2p, respectively. However, in comparison with LFP(R)-Ar, LFP(R)-CO_2, and LFP(C), the XPS full spectrum of LFP(S) exhibits the presence of F 1s, which disappears after high-temperature treatment, indicating the removal of impurities. Moreover, the peak heights of each element in LFP(C) and LFP(R)-CO_2 are higher than those in LFP(R)-Ar and LFP(S), respectively. This indicates that in a high-temperature environment filled with carbon dioxide gas, the carbon coating reacts with carbon dioxide, causing thinning or partial detachment of the carbon coating encapsulating the lithium iron phosphate, thus exposing the lithium iron phosphate. On the other hand, LFP(R)-Ar and LFP(S) are still covered by the carbon coating, preventing the exposure of $LiFePO_4$. As a result, X-rays can only detect carbon, leading to significant differences in peak heights.

The fine spectrum of the Fe element in XPS is depicted in Fig. 2c, where the main peaks at 711.75 eV and 709.84 eV in LFP(S) correspond to Fe^{3+} and Fe^{2+} of Fe $2P_{3/2}$, respectively, the main peaks at 724.53 eV and 723.25 eV correspond to Fe^{3+} and Fe^{2+} of Fe $2p_{1/2}$, respectively [42]. The quantification of Fe^{3+}/Fe^{2+} is achieved by determining the area ratio of the fitted peaks. Compared to LFP(S), the main peaks of Fe $2p_{3/2}$ and Fe $2p_{1/2}$ in LFP(R)-CO_2 and LFP(C) shift to higher binding energies. The peak area ratio of Fe^{3+}/Fe^{2+} changes from 1.181 in LFP(S) to 0.5677 in LFP(R)-CO_2, which is close to 0.558 in LFP(C). Meanwhile, in LFP(R)-Ar, the main peaks of Fe $2p_{3/2}$ and Fe $2p_{1/2}$ shift to lower binding energies. The peak area ratio of Fe^{3+}/Fe^{2+} is 1.0056, which is similar to the peak area ratio of Fe^{3+}/Fe^{2+} in LFP(S). H_2/Ar mixed gas, acting as a reducing atmosphere, facilitates the partial reduction of Fe^{3+} to Fe^{2+}. CO_2 gas reacts with the carbon coating to generate CO, which serves as a reducing atmosphere and reduces a significant portion of Fe^{3+} to Fe^{2+}, thereby reducing the content of Fe^{3+}. At the same time, as the carbon coating is thinned or partially removed, the lithium source successfully enters the corresponding crystal structure sites of LFP, the lithium ion diffusion channel is unblocked, the lithium-iron antisite defects are repaired, the lithium ion transfer kinetics are improved, and the spent LFP material is successfully repaired.

Performing X-ray diffraction (XRD) analysis on LFP(S), LFP(R)-Ar, LFP(R)-CO_2, and LFP(C). Fig. 2d illustrates the spectra of LFP(S), LFP(R)-Ar, and LFP(R)-CO_2, which are consistent with the stan-

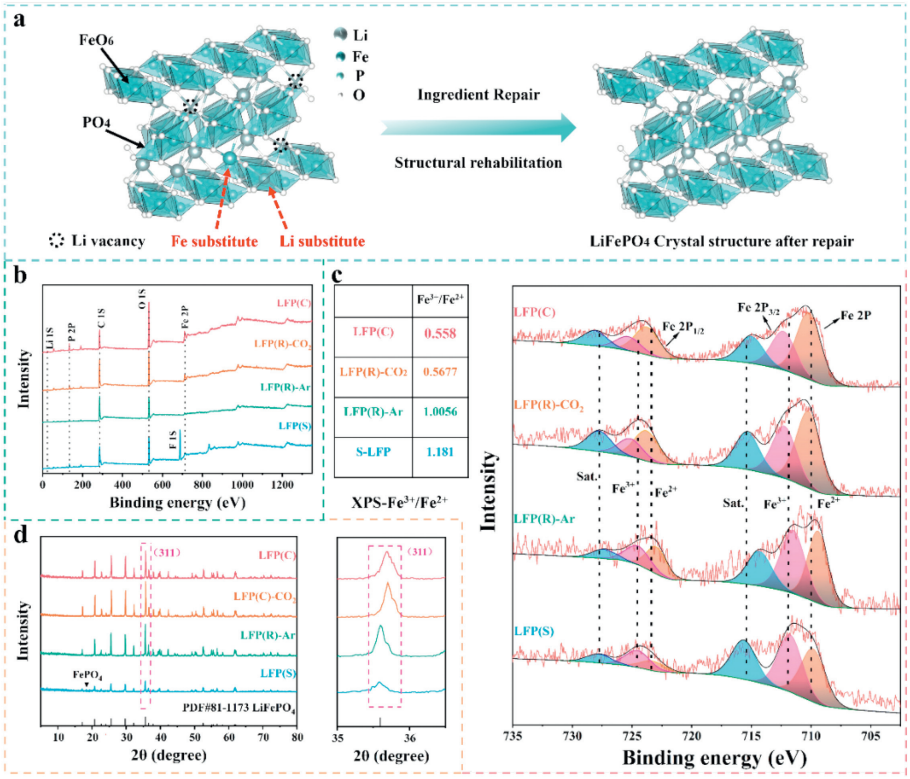

Fig. 2. (a) Failure mechanism diagram of LFP(S). (b) XPS full spectra of LFP(S), LFP(R)-Ar, LFP(R)-CO_2, and LFP(C). (c) Fe element XPS spectra and the peak area ratio of Fe^{3+}/Fe^{2+} for LFP(S), LFP(R)-Ar, LFP(R)-CO_2, and LFP(C). (d) XRD patterns of LFP(S), LFP(R)-Ar, LFP(R)-CO_2, and LFP(C), as well as an enlarged XRD pattern of the (311) crystal plane.

dard card ($LiFePO_4$, JCPDS No. 81–1173). From the XRD pattern, the main diffraction peak of LFP(S) is evident, indicating the preserved crystal structure of the discarded $LiFePO_4$. However, an impurity peak corresponding to the (020) crystal plane of $FePO_4$ appears at $2\theta = 18.153°$ in LFP(S). In contrast, this crystal plane is not observed in the LFP(R)-CO_2 sample, indicating a significant lithium deficiency in LFP(S). After undergoing high-temperature lithium replenishment treatment, the impurity phase is eliminated. Through the comparison of diffraction peak intensities, the intensity of the LFP(R)-CO_2 diffraction peak is significantly improved compared to LFP(S), and the LFP(R)-CO_2 diffraction peak intensity is essentially consistent with that of commercial $LiFePO_4$. This indicates that the crystallinity of $LiFePO_4$, treated in a high-temperature environment filled with CO_2 gas, has been improved and is now equivalent to that of commercial $LiFePO_4$. However, the crystallinity of $LiFePO_4$ treated in a high-temperature environment filled with Ar gas is inferior to that of $LiFePO_4$ treated in a high-temperature environment filled with CO_2 gas. As can be seen from the (311) crystal magnification spectrum, the LFP(R)-CO_2 peak is shifted to the right, close to the position of the main peak of commercial $LiFePO_4$, compared to LFP(S). In contrast to LFP(S), there is no significant change observed in the peak position of LFP(R)-Ar. According to the Bragg's equation, when the lattice spacing increases when the diffraction peak angle shifts to the left, and vice versa, the lattice spacing decreases, leading to a smaller lithium ion diffusion distance. After high-temperature treatment in an environment filled with carbon dioxide gas, the carbon coating was thinned or partially removed, resulting in successful lithium replenishment. Furthermore, with the application of high-temperature treatment, the lattice structure is restored. The interplanar spacing decreases compared to LFP(S), which shortens the lithium ion diffusion distance, leading to the successful restoration of the discarded LFP.

The surface characteristics of LFP(S), LFP(R)-Ar, LFP(R)-CO_2, and LFP(C) are shown in Fig. 3. Scanning electron microscopy (SEM) tests showed that LFP(C), in the absence of a carbon coating on its surface, had a smooth surface morphology (Fig. S3a in Supporting information), while the surface of commercial LFP, which was coated with a carbon layer, was obviously covered with a carbon coating (Fig. S3b in Supporting information). Fig. 3a regions I, II, and III of LFP(S), as well as the surface of commercial LFP coated with a carbon layer, showed a clearly uniform thick carbon layer on the surface. The surface morphology of LFP(R)-Ar was identical to that of LFP(S), but under the influence of CO_2, the surface of LFP(R)-CO_2 became smooth, and the carbon layer was significantly reduced and thinner compared to LFP(S). This indicates that CO_2 reacted fully with C, compared to LFP(R)-Ar, in the absence of a carbon coating prot ection, lithium ions can easily penetrate into LFP through the physical action of grinding, achieving the component restoration of waste LFP.

High-resolution transmission electron microscopy (HRTEM) images reveal the atomic-level microstructure of LFP particles [43]. Fig. 4a and Fig. S4a (Supporting information) show the TEM images of LFP(S), where the edges of LFP particles clearly contain a uniform carbon coating. The lattice spacing on the surface of LFP particles in Fig. 4b is measured to be 0.5166 nm, corresponding to the (200) plane of LFP. The surface region II of LFP particles in Fig. 4c reveals a disordered interface, indicating structural degradation. The magnified image of region I in Fig. 4d and Fig. S4b (Supporting information) show that after high-temperature treatment in an environment filled with argon gas, the surface of LFP remains uniformly coated with a carbon layer. However, after a high-temperature lithium replenishment treatment, the disordered region disappears, and the lattice spacing is measured to be 0.366 nm, corresponding to the (011) plane of LFP. The magnified image of region I in Fig. 4e and Fig. S4c (Supporting infor-

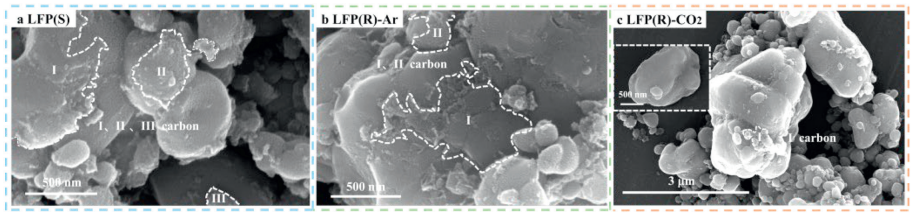

Fig. 3. (a) Scanning electron microscopy image of LFP(S). (b) Scanning electron microscopy image of LFP(R)-Ar. (c) Scanning electron microscopy image of LFP(R)-CO_2.

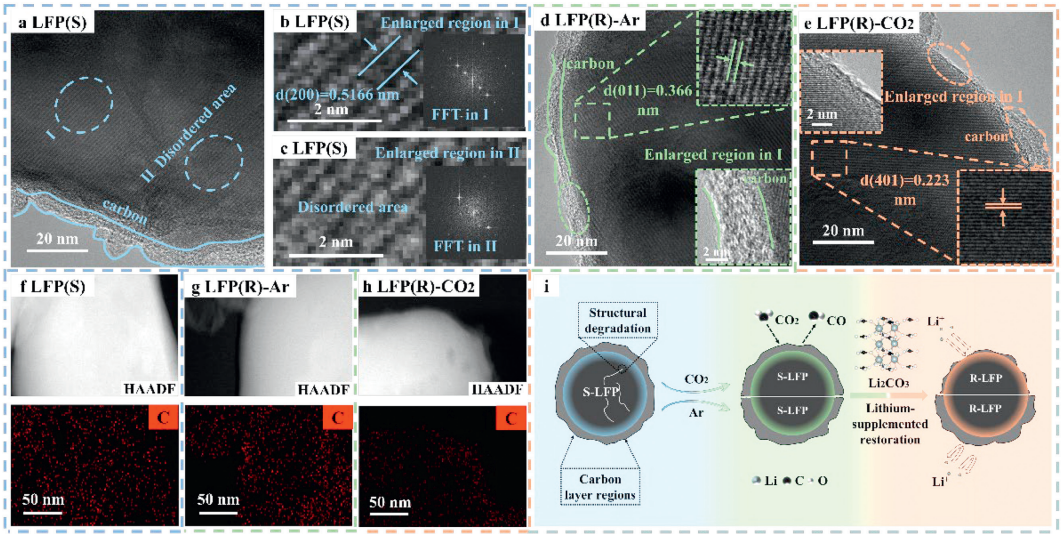

Fig. 4. (a-c) Transmission electron microscopy images of LFP(S). (d) Transmission electron microscopy images of LFP(R)-Ar. (e) Transmission electron microscopy image of LFP(R)-CO_2. (f) EDS elemental mapping image of LFP(S). (g) EDS elemental mapping image of LFP(R)-Ar. (h) EDS elemental mapping image of LFP(R)-CO_2. (i) Mechanism map of LFP(S) direct regeneration.

mation) shows that after high-temperature treatment in an environment filled with CO_2 gas, the carbon coating on the LFP surface has disappeared or has a thin thickness, the lattice spacing of 0.223 nm corresponds to the (401) crystal face of LFP. The lattice fringes on the LFP(R)-CO_2 surface have significantly enhanced clarity compared to LFP(S) and LFP(R)-Ar, and are no longer significantly different from the LFP(C) surface structure in Figs. S4d and S5 (Supporting information). By analyzing the EDS element maps (Figs. 2f–h) of LFP(S), LFP(R)-Ar and LFP(R)-CO_2, it can be seen that the surface carbon element content in LFP(R)-CO_2 significantly decreases. This indicates that CO_2 and the carbon coating undergo corresponding reactions, resulting in the thinning or partial removal of the carbon coating.

A comprehensive analysis of XRD, XPS, SEM, and TEM data reveals the regeneration mechanism of spent LFP (Fig. 4i). When high-temperature calcination in an Ar gas-filled environment, there is no impact on the carbon coating. Brief mechanical grinding cannot adequately contact the lithium source with the spent cathode material, and the problem of lithium deficiency in the cathode material cannot be resolved. However, during high-temperature calcination in a carbon dioxide-rich environment, the carbon coating is partially removed. After brief mechanical grinding, the lithium source can make full contact with the cathode material, and the problem of lithium deficiency in the cathode material can be solved. In addition, the crystal structure is also reconstructed and repaired, and the content of Fe^{3+} is significantly reduced. Thinning or partial removal of the carbon coating facilitates the entry of lithium ions during the lithium repletion phase, which has significant advantages over traditional lithium repletion methods.

The current density 1 C long-cycling behavior of LFP(S), LFP(R)-Ar, LFP(R)-CO_2, and LFP(C) in the voltage range of 2.8–4.2 V is shown in Fig. 5a. Compared to LFP(S) and LFP(R)-Ar, LFP(R)-CO_2 exhibits superior stability, with a maximum discharge capacity of up to 131.2 mAh/g, and a reversible capacity of 116.3 mAh/g still remaining after 400 cycles. In comparison, the discharge specific capacity of LFP(S) and LFP(R)-Ar is lower and the capacity retention rate is poor, which may be due to the low content of lithium ions, the formation of Li^+/Fe^{2+} anti-isomeric structures, causing blockage of lithium ion diffusion channels, leading to stagnation of diffusion kinetics. Figs. S6a and b (Supporting information) show the charge-discharge curves of S-LFP and LFP(R)-CO_2 at a 1 C current density for different times. which are typical characteristic of flat voltage plateau relating to the reverse reaction of Fe^{2+}/Fe^{3+} couple and coincide well with the CV results. Furthermore, a significant polarization phenomenon was observed in LFP(S) during the first 100 cycles, and the curves of the regenerated samples almost overlap, indicating its superior cycling stability and electrochemical reversibility.

Fig. 5b displays the rate capability of LFP(S), LFP(R)-Ar, LFP(R)-CO_2, and LFP(C) from current density 0.1 C to 2 C. The discharge specific capacities of LFP(R)-CO_2 at 0.1, 0.2, 0.5, 1, and 2 C are 149.1, 139.2, 131.5, 121.8, and 106.1 mAh/g, respectively. At the same current density, the discharge specific capacity of LFP(R)-CO_2 is higher than that of LFP(S) and LFP(R)-Ar, and slightly lower than that of LFP(C). However, due to thinning or partial removal of the carbon coating, the capacity retention of LFP(R)-CO_2 decreases when the rate is restored to 0.2 C. Figs. S6c and d (Supporting information) show the charge-discharge curves of LFP(S) and LFP(R)-CO_2 at different current densities. After the regeneration treatment, the polarization phenomenon was significantly reduced, indicating the successful insertion of lithium ions, unblocking of lithium ion diffusion channels, and the repair and recrystallization of the LFP

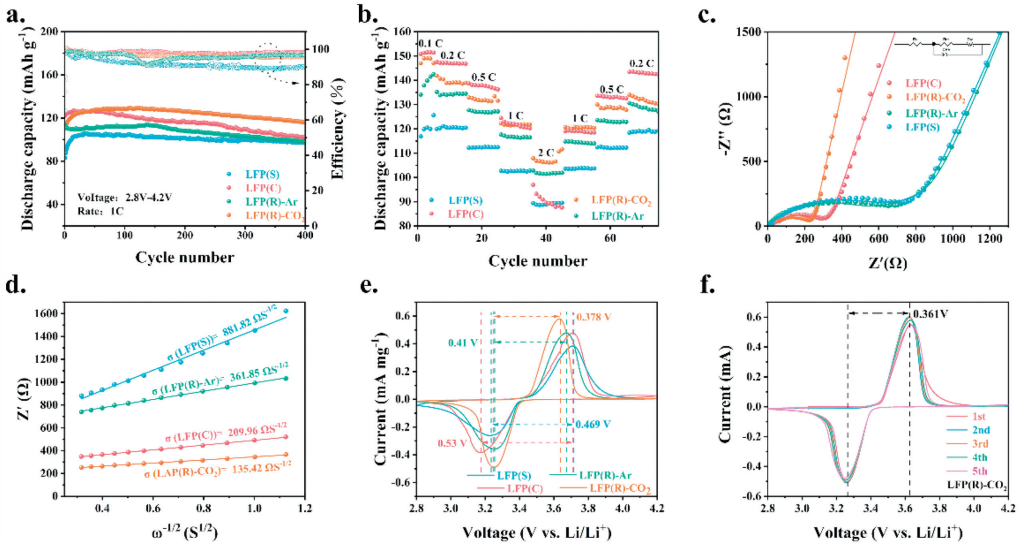

Fig. 5. (a) Long-term cycling curves of LFP(S), LFP(R)-Ar, LFP(R)-CO_2, and LFP(C) at 1 C. (b) Rate curves of LFP(S), LFP(R)-Ar, LFP(R)-CO_2, and LFP(C) at different current densities. (c) Nyquist plots of LFP(S), LFP(R)-Ar, LFP(R)-CO_2, and LFP(C). (d) Corresponding linear fits of the Z' and $\omega^{-1/2}$ values for the LFP(S), LFP(R)-Ar, LFP(R)-CO_2, and LFP(C) electrodes. (e) CV curves of LFP(S), LFP(R)-Ar, LFP(R)-CO_2, and LFP(C) electrodes at a scan rate of 0.2 mV/s. (f) The first 5 cycles of CV curves for the LFP(R)-CO_2 electrode at a scan rate of 0.2 mV/s.

Table 1
Equivalent circuit fitting.

Sample	R_s (Ω)	R_{ct} (Ω)
LFP(S)	10.29	585.7
LFP(R)-CO_2	9.875	213.5

structure. The successful recovery of LFP in XRD, XPS, and TEM mentioned above is also confirmed.

In addition, we also conducted EIS tests on LFP(S), LFP(R)-Ar, LFP(R)-CO_2, and LFP(C). All the ac impedance plots of the samples show a concave semi-circle related to charge transfer resistance (R_{ct}) in the high- and mid-frequency regions, and a linear graph related to the σ impedance (W_s) of lithium ion diffusion in the low-frequency region in Fig. 5c [44]. Table 1 shows that the R_{ct} of LFP(R)-CO_2 is smaller than LFP(S) [45], which proves that the charge transfer efficiency of the LFP(R)-CO_2 electrode is higher and the lithium ion diffusion kinetics is faster. This may be due to the successful repair of components and lattice in LFP(R)-CO_2, which unblocks the lithium ion diffusion channels and reduces resistance. Simultaneously, the ion diffusion coefficient (D_{Li^+}) can be expressed by the formula: $D_{Li^+} = R^2T^2/2A^2n^4F^4c^2\sigma^2$, where σ is inversely proportional to D_{Li^+}. D_{Li^+} is the inverse square root of the slope of the actual resistance and the low-frequency region angular frequency. As expected, the σ value of LFP(R)-CO_2 is the lowest (135.42), but the D_{Li^+} is the highest, which is higher than both LFP(R)-Ar (361) and LFP(S) (881.82) (Fig. 5d). This result confirms that resolving the lithium deficiency and structural reconstruction contribute to enhancing electronic conductivity and charge diffusion.

The cyclic voltammetry (CV) of LFP(S), LFP(R)-Ar, LFP(R)-CO_2, and LFP(C) in the voltage range of 2.8–4.2 V is shown in Fig. 5e. All the CV curves of the samples exhibit a pair of similar cathode-anode peaks, which correspond to the oxidation–reduction reactions of Fe^{2+}/Fe^{3+}, respectively. The potential difference between the oxidation peak and reduction peak for LFP(S), LFP(R)-Ar, LFP(R)-CO_2, and LFP(C) is 0.469, 0.41, 0.378, and 0.53 V, respectively. Due to the absence of a carbon coating on the surface, LFP(C) has poor conductivity, resulting in a larger polarization resistance and the maximum potential difference. In comparison, LFP(R)-CO_2 has the smallest potential difference among LFP(S), LFP(R)-Ar, and LFP(R)-CO_2, indicating lower electrode polarization. This suggests that Li^+ ions are more easily extracted and inserted, indicating better electrochemical performance. Simultaneously, the oxidation–reduction peaks of the LFP(R)-CO_2 electrode are sharper, narrower, more symmetrical, and exhibit the highest peak current compared to other similar electrodes. The electrochemical kinetics of LFP(R)-CO_2 are improved, charge diffusion is accelerated, and electrode polarization is reduced, which can be attributed to the presence of a partial carbon coating in LFP(R)-CO_2, which still retains a certain conductivity. Additionally, the lithium deficiency issue is resolved, filling the vacant lithium ions and unblocking the lithium ion diffusion channels. The structure of the phosphate lithium iron material is repaired and the lattice recrystallizes. Fig. 5f shows that the positions and corresponding intensities of the first five peaks in the CV curve of LFP(R)-CO_2 remain stable, while those of the LFP(S) CV curve in Fig. S7 (Supporting information) are unstable. This indicates that the reversibility issue in LFP(S) has been resolved, and the regenerated LFP possesses high reversibility. This also suggests that the cycling performance of LFP(R)-CO_2 is superior to that of LFP(S).

The large-scale application potential of thinning or partial removal of carbon coating in high-temperature, CO_2-rich environment for the recovery of spent lithium iron phosphate cathode materials is evaluated through economic benefit analysis. The details are shown in Tables S2 and S3 (Supporting information). The results indicate that the economic benefit of recovering 2 kg of spent lithium iron phosphate cathode material is $3.7512. Compared to traditional solid-phase regeneration methods, significant energy savings can be achieved during the Li_2CO_3 and LFP(S) blending stage. Therefore, this process can achieve significant economic benefits in the restoration and recovery of spent lithium iron phosphate materials.

In summary, we have improved the traditional solid-state regeneration method for the repair of lithium iron phosphate materials, successfully repairing spent lithium iron phosphate in a more environmentally friendly and cost-effective manner. The regeneration of used LFP materials involves a series of steps, including high-temperature separation, impurity removal, solid-phase grinding lithiation, and heat treatment. After electrochemical and char-

acterization tests, it was confirmed that the problem of missing lithium in the LFP material has been solved by means of lithium replenishment by solid-phase milling and that the structure has been restored and the crystallinity has been improved under high-temperature treatment. The lack of lithium in the long cycle of the used LFP caused the formation of Fe^{3+}, and after regeneration, the content of Fe^{3+} decreased significantly, and thus the electrochemical performance of the battery was improved accordingly. The regenerated LFP exhibits a capacity of 149.1 mAh/g at 0.1 C, which is almost identical to the performance of the original LFP without the carbon coating. The recovered LFP material can be reintroduced into the market, successfully providing an effective method for the disposal of spent LIBs.

Acknowledgment

This work was supported by Heilongjiang Province Key R&D Program (No. GA22A014).

Supplementary materials

Supplementary material associated with this article can be found, in the online version, at doi:10.1016/j.cclet.2024.110041.

References

[1] M. Fan, X. Chang, Y.J. Guo, et al., Energy Environ. Sci. 14 (2021) 1461–1468.
[2] Q. Liang, F. Chen, S. Wang, et al., Energy Storage Mater. 20 (2019) 203–207.
[3] X. Ma, M. Chen, Z. Zheng, et al., Joule 5 (2021) 2955–2970.
[4] C.M. Costa, J.C. Barbosa, R. Gonçalves, et al., Energy Storage Mater. 37 (2021) 433–465.
[5] L. Liang, X. Sun, J. Zhang, et al., Adv. Energy Mater. 9 (2019) 1802847.
[6] W. Zhang, L. Liang, F. Zhao, et al., Electrochim. Acta 340 (2020) 135871.
[7] X.G. Yang, T. Liu, C.Y. Wang, Nat. Energy 6 (2021) 176–185.
[8] A. Zhu, X. Bian, W. Han, et al., Resour. Conserv. Recy. 188 (2023) 106690.
[9] X. Guo, J. Zhang, Q. Tian, Renew. Sustain. Energy Rev. 137 (2021) 110461.
[10] K. Du, E.H. Ang, X. Wu, et al., Energy Environ. Mater. 5 (2022) 1012–1036.
[11] R. Bird, Z.J. Baum, X. Yu, et al., ACS Energy Lett. 7 (2022) 736–740.
[12] E. Fan, L. Li, Z. Wang, et al., Chem. Rev. 120 (2020) 7020–7063.
[13] J. Wang, K. Jia, J. Ma, et al., Nat. Sustain. 6 (2023) 797–805.
[14] G. Harper, R. Sommerville, E. Kendrick, et al., Nature 575 (2019) 75–86.
[15] J. Wang, J. Ma, K. Jia, et al., ACS Energy Lett. 7 (2022) 2816–2824.
[16] W. Lv, Z. Wang, H. Cao, et al., ACS Sustain. Chem. Eng. 6 (2018) 1504–1521.
[17] X. Zhang, L. Li, E. Fan, et al., Chem. Soc. Rev. 47 (2018) 7239–7302.
[18] X. Li, B. Wu, H. Sun, et al., Sustain. Energ. Fuel. 8 (2024) 1438–1447.
[19] T. Liu, Y. Zhang, C. Chen, et al., Nat. Commun. 10 (2019) 1965.
[20] F. Larouche, F. Tedjar, K. Amouzegar, et al., Mater 13 (2020) 801.
[21] Q. Liang, H. Yue, S. Wang, et al., Electrochim. Acta 330 (2020) 135323.
[22] J. Li, G. Wang, Z. Xu, J. Hazard. Mater. 302 (2016) 97–104.
[23] Y. Yang, X. Zheng, H. Cao, et al., ACS Sustain. Chem. Eng. 5 (2017) 9972–9980.
[24] T. Or, S.W.D. Gourley, K. Kaliyappan, et al., Carbon Energy 2 (2020) 6–43.
[25] A. Zhu, X. Bian, W. Han, et al., Waste Manage. 156 (2023) 139–147.
[26] K. Jia, J. Ma, J. Wang, et al., Adv. Mater. 35 (2023) 2208034.
[27] D. Tang, G. Ji, J. Wang, et al., Adv. Mater. 36 (2024) 2309722.
[28] X. Li, J. Zhang, D. Song, et al., J. Power Source 345 (2017) 78–84.
[29] X. Chen, S. Li, Y. Wang, et al., Waste Manage. 136 (2021) 67–75.
[30] J. Wang, Q. Kang, J. Yuan, et al., Carbon Energy 3 (2021) 153–166.
[31] M. Sha, L. Liu, H. Zhao, et al., Carbon Energy 2 (2020) 350–369.
[32] H. Ji, J. Wang, J. Ma, et al., Chem. Soc. Rev. 52 (2023) 8194–8244.
[33] P. Xu, Q. Dai, H. Gao, et al., Joule 4 (2020) 2609–2626.
[34] K.Y. Park, I. Park, H. Kim, et al., Chem. Mater. 26 (2014) 5345–5351.
[35] J. Henschel, F. Horsthemke, Y.P. Stenzel, et al., J. Power Source 447 (2020) 227370.
[36] J. Vetter, P. Novák, M.R. Wagner, et al., J. Power Source 147 (2005) 269–281.
[37] L. Yang, K. Yang, J. Zheng, et al., Chem. Soc. Rev. 49 (2020) 4667–4680.
[38] H. Liu, M.J. Choe, R.A. Enrique, et al., J. Phys. Chem. C 121 (2017) 12025–12036.
[39] G. Ji, J. Wang, Z. Liang, et al., Nat. Commun. 14 (2023) 584.
[40] C. Liu, J. Lin, H. Cao, et al., J. Clean. Prod. 228 (2019) 801–813.
[41] X. Han, L. Lu, Y. Zheng, et al., eTransportation 1 (2019) 10005.
[42] X. Wang, Z. Feng, X. Hou, et al., Chem. Eng. J. 379 (2020) 122371.
[43] Z. Gong, Z. Li, P. Wang, et al., Adv. Energy Mater. 4 (2023) 0035.
[44] Q. Li, Y. Zhao, H. Liu, et al., ACS Nano 13 (2019) 11921–11934.
[45] J. Zhang, X. Li, D. Song, et al., J. Power Source 390 (2018) 38–44.